

● *Original Contribution*

A NUMERICAL STUDY OF RADIOFREQUENCY DEPOSITION IN A SPHERICAL PHANTOM USING SURFACE COILS

RICHARD J. STRILKA,* SHIZHE LI,* JACK T. MARTIN,†,‡ CHRISTOPHER M. COLLINS,*
AND MICHAEL B. SMITH*†

Departments of *Radiology (Division of NMR Research), †Cellular and Molecular Physiology, The Pennsylvania State University College of Medicine, Hershey, PA; and the ‡Department of Radiology, Penn State Geisinger Health System, Danville, PA, USA

The electromagnetic fields induced by a surface coil in a spherical phantom, having a wide range of electrical properties, is studied using numerical methods of calculation. The specific absorption rate (SAR), radiofrequency magnetic field (B_1), magnetic field energy within the phantom (E_B), and the volume-averaged SAR ($\langle \text{SAR} \rangle$) are calculated at 10, 63, and 200 MHz. They are analyzed with respect to dielectric constant, wavelength, and skin depth effects, which become increasingly important in high field magnetic resonance imaging (MRI) where safety and field homogeneity issues need further study. Particular attention is given to solutions representing neural tissue at each frequency. In general, the $\langle \text{SAR} \rangle$ data at high field strengths have local maxima, with a quasi-harmonic behavior, when the following two resonant conditions are satisfied: 1) skin depth becomes comparable to, or larger than, the sample diameter D_s ; and 2) D_s is near an integral multiple of the wavelength. These are also the solutions with maximum E_B values and the least homogeneous B_1 . Samples undergoing resonance at 200 MHz are shown to have important off-axis B_1 maxima (affecting field homogeneity) and large $\langle \text{SAR} \rangle$ values. Some non-resonating 200-MHz phantoms, including simulations consistent with neural tissue, contain larger SAR maxima than the resonating samples, posing safety concerns in high field imaging of biologic tissue. © 1998 Elsevier Science Inc.

Keywords: SAR; Field homogeneity; Surface coils; Computer simulation.

INTRODUCTION

The radiofrequency (RF) magnetic (B_1) field homogeneity and the specific absorption rate (SAR) are important factors in magnetic resonance imaging (MRI). The B_1 field homogeneity directly affects profiles of image intensity and high SAR indicates RF power deposition levels inside the sample that may cause RF heating damages in biologic tissue. These two important subjects have been extensively studied with analytical, computational, and experimental methods.

Analytical methods can be used to investigate electromagnetic (EM) field properties for simple and symmetric geometries. For example, cylindrical models have been used to evaluate RF deposition¹⁻⁴ and B_1 field distributions.⁴⁻⁶ Analytical calculations have also been ap-

plied in semi-infinite space or multi-layer systems.^{2,5,7,8-10} Non-dominant terms in the full physics theory are commonly dropped to simplify equations that allow the analytic solutions to be tractable. The more reliable results, however, are found when the full set of physics equations are solved with a configuration that accurately resembles MRI in clinical practice. Electromagnetic field solutions are dependent upon the sample's geometric shape,¹¹ which has recently motivated the construction of more realistic three dimensional human head models used in the numerical calculations of the B_1 field at 64 MHz.¹²

Spherical models are often used as a first approximation of the human head in MRI. The B_1 field has been studied for spheres in plane waves,^{2,5,13} and for spheres near a surface coil.¹³⁻¹⁵ They have also been used to

RECEIVED 6/17/97; ACCEPTED 1/2/98.

Address correspondence to Dr. M. Smith, Penn State University College of Medicine, The Milton S. Hershey Medical

Center, Department of Radiology, P.O. Box 850, Hershey, PA, 17033, USA.

predict SAR levels at different frequencies.^{1,2,7,13,14,16-21} In early power deposition studies, the microwave range was used primarily. The physics theory, however, is essentially unchanged for RFs. For example, the RF power deposition in a spherical sample has been studied by using a uniform external electromagnetic field and applying the quasi-static field assumption outside the sample where the wavelength is taken to be much larger than the sphere's diameter.^{1,2,13,17,20,21} These conditions are chosen to simplify the equations and solutions. This approximation is more appropriate for a sample placed inside a large RF volume coil running at low frequency, but less accurate for the sample placed next to a surface coil at high frequency. Carlson has shown the power distribution in a 30-cm diameter sphere next to a surface coil with an approximate solution at frequencies from 10 to 150 MHz,¹³ and with an exact solution at frequencies from 200 to 400 MHz.¹⁴ Only a few SAR values, however, were calculated at particular points along the configuration's axis of symmetry. The SAR throughout the sphere was not presented.

In high field configurations, previously unimportant low field phenomena, such as dielectric resonance, begin asserting effects on the field homogeneity, SAR, and volume-averaged SAR. In coil design, it is important to evaluate accurately the coil's RF field strength and the resultant inductive losses under such circumstances. Typically, the approximations within the analytical calculations used to study these effects become increasingly unreliable at high frequencies.

This work applies finite element methods to calculate RF field behaviors for a spherical sample next to a single-turn surface coil at 10, 63, and 200 MHz. The simulation geometry is identical to that studied analytically by Carlson and Keltner et al.^{13,14} RF field behaviors studied include deposition of electric power, total magnetic energy inside the sphere, and spatial distributions of the B_1 field magnitude and SAR across the sphere. The full set of Maxwell's equations are solved, allowing accurate solutions for a wide variety of sample conductivity and permittivity (90 combinations for each frequency) to cover a large number of possible tissue characteristics, as well as non-biologic combinations of conductivity and permittivity. This effort compliments previous studies by a) solving the complete set of Maxwell's equations (without using a quasi-static or long wavelength approximation) for the entire system; b) presenting general patterns of averaged SAR and total magnetic energy as a function of frequency from a large enough variation of a sample's conductivity (and relative permittivity ϵ_r , including non-biologic σ and ϵ_r , to study general wavelength and skin depth effects; and c) displaying the B_1 field magnitude and SAR across the sphere's cross-section, allowing more accurate conclu-

sions concerning dielectric effects than afforded by previous analytical solutions.^{13,14}

MATERIALS AND METHODS

Model and Numerical Techniques

The computer simulations were performed on an IBM RISC 6000, model 550 workstation using a complete Maxwell equation field solver (Ansoft Corp., Pittsburgh, PA, USA) running on an AIX operating system. This software has successfully calculated static and RF magnetic fields and correctly considers both displacement and eddy current contributions.²²⁻²⁴ The user defines the model geometry and assigns the material properties to the phantom and RF coil. The finite element method used solves for the vector potential \mathbf{A} by using the following equation:

$$\frac{1}{\mu} \nabla \times \nabla \times \mathbf{A} = (\sigma + j\omega\epsilon)(-j\omega\mathbf{A} - \nabla\varphi) \quad (1)$$

where μ is the permeability, ϵ is the permittivity, σ is the conductivity, φ is the electric scalar potential, ω is the angular frequency, and $j^2 = -1.0$. The magnetic induction \mathbf{B} is calculated as

$$\mathbf{B} = \nabla \times \mathbf{A} \quad (2)$$

The right hand side of Eq. (1) is the total current density, \mathbf{J}_t , which is the vector sum of the "source" current density, $\mathbf{J}_s = -\sigma \nabla \varphi$, the eddy current density, $\mathbf{J}_e = -j\omega\sigma\mathbf{A}$, and the displacement current density, $\mathbf{J}_d = j\omega\epsilon(-j\omega\mathbf{A} - \nabla\varphi)$.

The configuration simulated was a spherical sample placed next to a single turn surface coil with a 2-mm wire thickness. The sample diameter D_s was 30 cm and the coil diameter was 15 cm. The coil was symmetrically placed 2 cm above the sphere and carried 2.0 amps of alternating current. Cylindrical coordinates were used to solve Eq. (1) because of the configuration's manifest angular symmetry. The z -axis was chosen to define the line of revolution of the coil and sphere. All currents would then be circulating with only an azimuthal component. Eq. (2) then defines a \mathbf{B} vector field with only radial and z -components, which effectively makes the problem two dimensional in the r - z -plane and more manageable computationally. The coil and sample was centered at the origin of the computational box with side lengths 20.0×10.0 m in the r - z -plane. The vector potential \mathbf{A} was set to zero along the boundaries because the magnetic field rapidly vanishes far from the coil center. The computational box was tiled with a non-uniform 13,500 triangular mesh that was more refined within the phantom and the region surrounding the coil

so that skin depth and dielectric effects would be well represented.

The frequencies of 10, 63, and 200 MHz were used in the calculations. The phantom's electrical properties were chosen by defining nine σ values (from 0.15 to 1.35 S/m with increments of 0.15 S/m) and 10 relative permittivity values (ϵ_r from 1.00 to 405 with increments of 45). The relative permittivity ϵ_r is related to ϵ via $\epsilon = \epsilon_o \epsilon_r$, where ϵ_o is the vacuum permittivity. Solutions to Eq. (1) were then calculated for each of the 90 different combinations of σ and ϵ_r at each frequency. This extensive collection of 270 total solutions represents a broad range of possible material characteristics. The computer time needed to solve each simulation varied considerably. Generally, samples undergoing resonance at higher frequencies were the most computationally intensive, requiring 24–96 h to converge to a solution. Conversely, a simulation at 10 MHz, for example, required approximately 10 min.

Solving Eq. (1) allows the calculation of the B_1 field, total magnetic energy, SAR, and volume-averaged SAR. The total magnetic energy stored inside the sample E_B was calculated by integrating the magnetic energy density over the volume of the spherical sample as:

$$E_B = \mu \int \mathbf{H}_1 \cdot \mathbf{H}_1 dv \quad (3)$$

where $H_1 = B_1/\mu$. The SAR is defined as:

$$\text{SAR} = \frac{\sigma}{2\rho} E^2 \quad (4)$$

where ρ is the density of the material and E is the peak value of the electric field. The SAR corresponds to the electric power in a unit mass of tissue. Equivalently, the software package uses the eddy current density to define the SAR as:

$$\text{SAR} = \frac{1}{2\sigma\rho} J_e^2 \quad (5)$$

where J_e is the peak value of the eddy current. Using Eq. (5), the volume-averaged SAR, $\langle \text{SAR} \rangle$, was calculated for the entire spherical sample by applying the following equation:

$$\langle \text{SAR} \rangle = \frac{\int \frac{1}{2\sigma} J_e^2 dv}{\int \rho dv} \quad (6)$$

Thus, $\langle \text{SAR} \rangle$ is proportional to the total electrical power deposited inside the sphere. (The density of water, $\rho = 1000 \text{ kg/m}^3$, was used for all the calculations.)

The simulation results were dependent on the wavelength within the samples λ and the skin depth of the material δ . These quantities are functions of frequency and the material's electrical parameters, and are defined in the following equations:

$$\delta = \frac{1}{\omega \sqrt{\frac{\mu\epsilon}{2} \left[\sqrt{1 + \left(\frac{\sigma}{\omega\epsilon}\right)^2} - 1 \right]^{1/2}}} \quad (7)$$

$$\lambda = \frac{2\pi}{\omega \sqrt{\frac{\mu\epsilon}{2} \left[\sqrt{1 + \left(\frac{\sigma}{\omega\epsilon}\right)^2} + 1 \right]^{1/2}}} \quad (8)$$

The values of ϵ and σ for different biologic tissues have been measured at different frequencies.^{25,26}

RESULTS AND DISCUSSION

The first subsection discusses how the simulations are related to experimentally derived data and FDA limits placed on SAR and $\langle \text{SAR} \rangle$. The second subsection presents the general trends of $\langle \text{SAR} \rangle$ and E_B . They are used to discuss dielectric resonance and are analyzed in terms of σ and ϵ_r . The final subsection contains cross-section surface plots of the SAR and $B_{1\rho}$ field magnitude ($B_{1\rho} = B_1/2$) for the solution most closely representing neural tissue at each frequency and the solutions undergoing strong dielectric resonance at 63 and 200 MHz. These field quantities are also analyzed in terms of σ and ϵ_r . For convenience, all configurations presented are grouped by frequency.

Relationship to Experiment and FDA SAR and $\langle \text{SAR} \rangle$ Limits

The single turn surface coil produces an oscillating B_1 field that is a linear combination of two circularly polarized components. The RF excitation used to create an image arises from only one of the circular components, called $B_{1\rho}$. For this reason, only the magnitude of $B_{1\rho}$, $B_{1\rho}$, which satisfies $B_{1\rho} = B_1/2$, is displayed below. The eddy current excitation, however, is still determined by the B_1 field and is related to SAR via Eq. (5), which describes the power absorbed for a single pulse. Thus, a change in the B_1 strength will necessarily induce a different SAR. To reasonably compare SAR between different samples, B_1 needs to be normalized. Accordingly, the reference point A was specified within each solution, located on the coil's axis 5 cm deep from the sphere surface, so that the magnitude of $B_{1\rho}$ at point A, $B_{1\rho}(A)$,

Table 1. The maximum and minimum λ and δ values in each frequency sample set. The σ and ϵ_r values where the maximum and minimum occur are listed under λ_{\max} , λ_{\min} , δ_{\max} , and δ_{\min}

Frequency (MHz)	λ_{\max} (cm) $\sigma = 0.15, \epsilon_r = 1.00$	λ_{\min} (cm) $\sigma = 1.35, \epsilon_r = 405$	δ_{\max} (cm) $\sigma = 0.15, \epsilon_r = 405$	δ_{\min} (cm) $\sigma = 1.35, \epsilon_r = 1.00$
10	257	79.2	74.7	13.7
63	102	21.7	71.3	5.46
200	55.6	7.37	71.2	3.08

could be normalized to 3.0 μT . This produces a 2.0 ms rectangular 90° RF pulse for a given nuclei at that point within all samples. Specifically, if $B_{1\rho}$ is reduced by a factor of two, the scaled SAR is decreased by four. The normalized SAR can then be compared directly with the same conditions.

The FDA limits on power absorption are 8.0 W/kg for SAR (within a gram of tissue) and 3.2 W/kg for $\langle\text{SAR}\rangle$.²⁷ Thus, experimental measurements of SAR are done over finite volumes whereas numerical methods, which use Eq. (5), determine SAR at any given spatial location. This implies that Eq. (5) provides an upper limit on what may be expected in experiment. The $\langle\text{SAR}\rangle$, because volume averaged, may be compared with experiment directly. In addition, the FDA limits restrict SAR and $\langle\text{SAR}\rangle$ values for a pulse sequence which is equal to the sum of energy absorbed from the pulses during the entire acquisition divided by the acquisition time.¹ For example, the SAR of a standard spin-echo sequence, $\text{SAR}_{\text{sequence}}$, will be:

$$\text{SAR}_{\text{sequence}} = \frac{\text{SAR}_{90} \times T^{90} + \text{SAR}_{180} \times T^{180}}{\text{TR}}, \quad (9)$$

where SAR_{90} and SAR_{180} are the SAR induced during a pulse with flip angles 90° and 180°, T^{90} and T^{180} are the respective pulse durations, and TR is the repetition time. For clarity, $\text{SAR}^{\text{pulse}}$ and $\langle\text{SAR}\rangle^{\text{pulse}}$ will henceforth be used when referring to the spatial distributed and volume-averaged SAR for a single pulse. Eq. (9) shows that $\text{SAR}^{\text{pulse}}$ and $\langle\text{SAR}\rangle^{\text{pulse}}$ are greater than SAR and $\langle\text{SAR}\rangle$ for a given sequence. The FDA limits on SAR and $\langle\text{SAR}\rangle$ are discussed throughout the remaining subsections.

The amount of temperature increase the sample experiences from the surface coil is in principle related to the SAR. The relationship, however, is non-trivial, requiring numerical methods that include the effects of blood flow and conductive losses on core temperature changes.²⁸ Furthermore, conditions such as room temperature, humidity, air circulation, or even patient attire, will cause the temperature results to vary widely. Thus, the SAR can be calculated with far greater confidence than values

of tissue temperature. For this reason, only the FDA safety recommendations for SAR, rather than FDA limits on temperature changes, are discussed.

General Trend of $\langle\text{SAR}\rangle$ and E_B

Equations (7) and (8) indicate that λ and δ decrease with increasing σ or ω ; whereas λ decreases and δ increases with increasing ϵ_r . This creates a complex dependence between the phantom's electrical properties and λ or δ . An important length scale is set by the sample diameter D_s . Consequently, the set of λ and δ included several values that were smaller, on the order of, and larger than D_s . The maximum and minimum values of λ and δ , for each frequency, are shown in Table 1. When $\delta < D_s$, the magnetic field produced by the coil decays rapidly as it enters the sample. Any resonant patterns will be damped and the resultant field inhomogeneities will not be appreciable. This result appears independent of λ and the EM field solution is characteristically simple in its spatial distribution. The situation is quite different when $\delta > D_s$. Here, when λ is small enough, the incident EM wave may reflect off the sphere/air interface, back into the phantom, with an amplitude sufficient to create a complex field pattern. The E_B is increased from constructive interference because B_1 is increased within certain parts of the sample, producing an inhomogeneous spatial distribution. The field complexity, created by interference, becomes particularly pronounced when λ approximates a fraction of the sample dimension, $D_s \cong n\lambda$. In these situations, the phantom absorbs the most EM energy from the coil, partly in the form of eddy currents, and is said to be undergoing dielectric resonance. In general, resonating samples have electrical parameters that satisfy both $D_s \cong n\lambda$ and $\delta > D_s$, consequently, they have relatively larger $\langle\text{SAR}\rangle^{\text{pulse}}$ and E_B values.

10-MHz Solutions

The shortest 10-MHz wavelength in Table 1 is 2.6 times larger than the sample diameter and the skin depths are shorter than D_s , except for solutions with $\sigma \leq 0.30$ S/m. Thus, no samples undergo dielectric resonance and the dependence of $\langle\text{SAR}\rangle^{\text{pulse}}$ on σ or ϵ_r is simple. Figure 1a shows several $\langle\text{SAR}\rangle^{\text{pulse}}$ vs. ϵ_r curves for

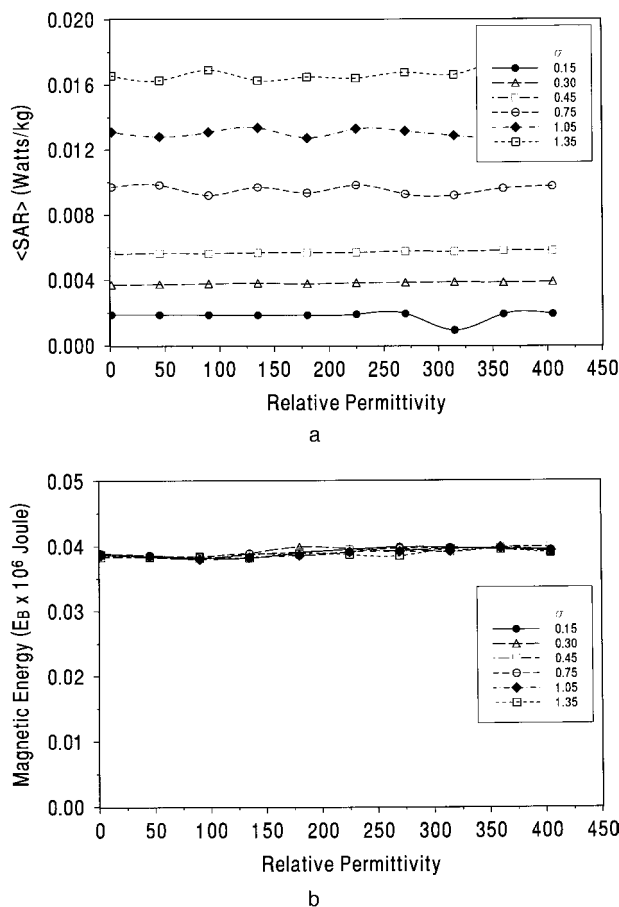


Fig. 1. (a) The $\langle \text{SAR} \rangle^{\text{pulse}}$ vs. ϵ_r , and (b) E_B vs. ϵ_r curves, for the 10-MHz simulations. The figure legends contain the σ values presented. The $\langle \text{SAR} \rangle^{\text{pulse}}$ and E_B curves demonstrate that B_1 is not perturbed by the phantom. Spline curves are used to interpolate between the data points with the same σ .

different σ . For clarity of presentation, samples with $\sigma = 0.60, 0.90,$ and 1.20 S/m have not been shown and a spline curve was used to approximately interpolate between data points within each ϵ_r series. Each curve is nearly flat, demonstrating that the $\langle \text{SAR} \rangle^{\text{pulse}}$ is approximately ϵ_r independent. Figure 1a also depicts a linear relationship between σ and $\langle \text{SAR} \rangle^{\text{pulse}}$, which is expected from Eq. (4) provided that the electric field inside the phantom is nearly the same for all samples; the coil in free space (without the phantom) solution. The maximum 10-MHz $\langle \text{SAR} \rangle^{\text{pulse}}$ value, $7.04\text{E-}2$ W/kg, occurs when $\sigma = 1.35$ S/m, and is well below the FDA 3.2-W/kg limit.

Figure 1b plots E_B vs. ϵ_r , for the same σ values used in Fig. 1a. All of the following 63 and 200-MHz $\langle \text{SAR} \rangle^{\text{pulse}}$ and E_B figures have the same format. All phantoms have approximately the same magnetic energy ($3.9\text{E-}2 \mu\text{J}$) reflecting the spatial similarity of the solutions. Such behavior results from λ being large compared

to D_s , so that the EM field produced by the coil is unaffected by the phantom.

63-MHz Solutions

At this frequency, the majority of the B_1 field wavelengths are nearly equal to D_s (30 cm), whereas σ ranges between 5 and 70 cm. Many phantoms consequently have $\langle \text{SAR} \rangle^{\text{pulse}}$ values that are an order of magnitude larger than their 10-MHz counterpart. The maximum 63-MHz $\langle \text{SAR} \rangle^{\text{pulse}}$ value occurs when $\sigma = 0.15$ S/m and $\epsilon_r = 250$ and is 0.93 W/kg. The $\langle \text{SAR} \rangle^{\text{pulse}}$ vs. ϵ_r plots, Fig. 2a, shows that the $\langle \text{SAR} \rangle^{\text{pulse}}$ values generally increase with σ and ϵ_r . The $\langle \text{SAR} \rangle^{\text{pulse}}$ curves with $\sigma = 0.15$ and 0.30 S/m are more complex and contain a local maximum near $\epsilon_r = 270$. The range of ϵ_r over which $\langle \text{SAR} \rangle^{\text{pulse}}$ values become significantly large is 180 to 300, indicating that these phantoms are near dielectric resonance. The resonating samples ($\sigma = 0.15$

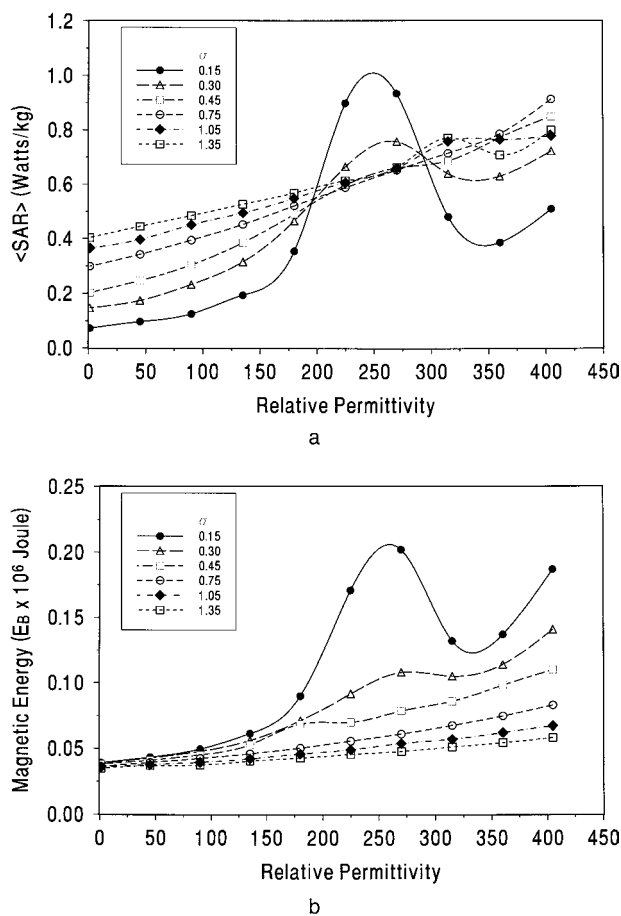


Fig. 2. (a) The $\langle \text{SAR} \rangle^{\text{pulse}}$ vs. ϵ_r , and (b) E_B vs. ϵ_r curves, for the 63-MHz simulations. The $\sigma = 0.15$ and 0.30 S/m $\langle \text{SAR} \rangle^{\text{pulse}}$ and E_B curves obtain a local maxima where σ and ϵ_r values yield $\lambda \cong D_s$.

and $\epsilon_r = 270$) absorb the most energy from the coil and have σ and ϵ_r values which yield $\lambda \cong D_s \cong 30$ cm and $\delta > D_s$. In regions where $\epsilon_r < 180$ or > 315 , the $\sigma = 0.15$ and 0.30 S/m $\langle \text{SAR} \rangle^{\text{pulse}}$ curves generally resemble those plots with $\sigma > 0.30$ S/m by increasing in a monotonic fashion with ϵ_r while still being approximately proportional to σ . Figure 2a shows that increasing ϵ_r , resulting in shorter λ and longer σ values, allows the samples to absorb more EM energy. If δ is shorter than D_s ($\sigma > 0.30$ S/m), the resonance effects are suppressed regardless of λ and no significant $\langle \text{SAR} \rangle^{\text{pulse}}$ peaks are observed.

The E_B vs. ϵ_r curves in Fig. 2b behave similar to the $\langle \text{SAR} \rangle^{\text{pulse}}$ graphs (Fig. 2a) in that they also generally increase with σ and ϵ_r and obtain local maximum at the same ϵ_r values along the $\sigma = 0.15$ and 0.30 S/m curves. The E_B curves differ from the $\langle \text{SAR} \rangle^{\text{pulse}}$ graphs in that at lower σ or ϵ_r , the E_B are strictly smaller than E_B at the higher σ or ϵ_r . Furthermore, solutions corresponding to the E_B peaks in the $\sigma = 0.15$ and 0.30 S/m curves undergoing dielectric resonance have complex B_1 field patterns with non-trivial B_1 maxima inside the sample, increasing the E_B value. Thus at 63 MHz, MRI image intensity variations may be largest in those samples with $\lambda \cong D_s \cong 30$ cm and $\delta > D_s$.

200-MHz Solutions

At this frequency, 77 of the 90 solutions have $\lambda < D_s$ with skin depths ranging from 3.0 to 29.0 cm. Similar to the 63-MHz configurations, dielectric resonance only occurs for particular solutions, here within the $\sigma = 0.15$, 0.30 , and 0.45 S/m group, where $\lambda \cong 15$, 10 , and 7.5 cm, respectively, and $\delta > D_s$. In general, the 200-MHz $\langle \text{SAR} \rangle^{\text{pulse}}$ values are almost an order of magnitude larger than their 63-MHz counterparts with a maximum of 5.75 W/kg when $\sigma = 0.15$ S/m and $\delta_r = 75$. The $\langle \text{SAR} \rangle^{\text{pulse}}$ vs. ϵ_r plots, Fig. 3a, have local maxima appearing on the $\sigma = 0.15$, 0.30 and 0.45 S/m curves. In particular, the $\sigma = 0.15$ S/m curve has three maxima when $\epsilon_r = 90$, 225 , and 405 which corresponds to the approximate wavelengths of $D_s/2$, $D_s/3$, and $D_s/4$, respectively. The maxima on the $\sigma = 0.30$ and $\sigma = 0.45$ S/m curves have similar wavelength correspondences. For the curves with higher σ values, the EM field is effectively damped by the shorter skin depth and the $\langle \text{SAR} \rangle^{\text{pulse}}$ curves gradually become smoother.

Similar to the 63-MHz simulations, the E_B vs. ϵ_r curves, Fig. 3b, have local maxima occurring at the same ϵ_r values as the $\langle \text{SAR} \rangle^{\text{pulse}}$ curves had maxima. All E_B values at smaller σ or ϵ_r are strictly less than those E_B values at larger σ or ϵ_r . The B_1 field corresponding to these local E_B maxima have complex spatial patterns. The largest $\langle \text{SAR} \rangle^{\text{pulse}}$ value ($\sigma = 0.15$ S/m and $\epsilon_r = 75$) does not correspond to the largest E_B value ($\sigma = 0.15$

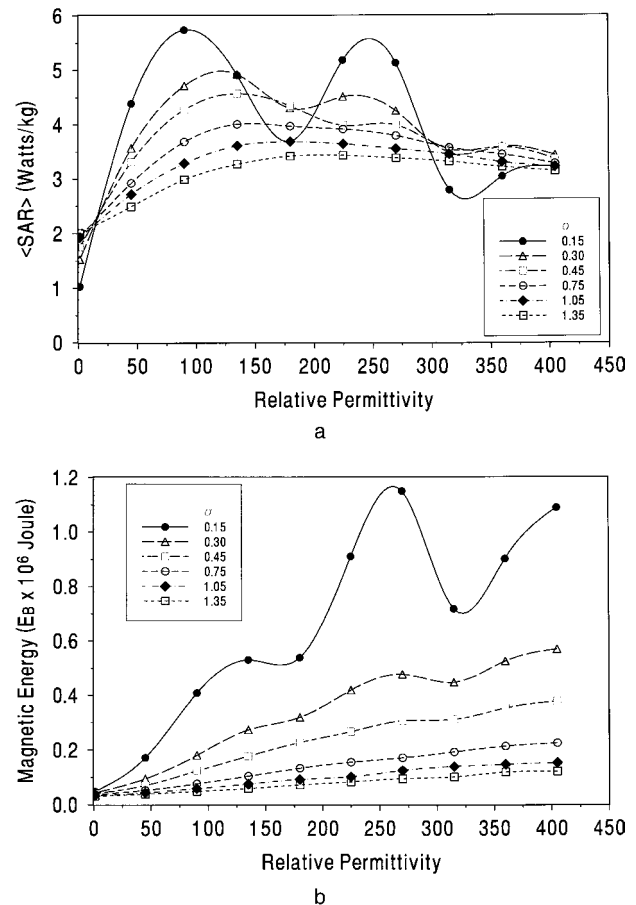


Fig. 3. (A) The $\langle \text{SAR} \rangle^{\text{pulse}}$ vs. ϵ_r , and (B) E_B vs. ϵ_r curves, for the 200-MHz simulations. The $\sigma = 0.15$, 0.30 , and 0.45 S/m $\langle \text{SAR} \rangle^{\text{pulse}}$ and E_B curves obtain three local maxima where σ and ϵ_r values yield $\lambda \cong D_s/2$, $D_s/3$, and $D_s/4$.

S/m and $\epsilon_r = 275$). Thus, configurations with the greatest B_1 field inhomogeneities (possibly producing images with large variations in intensity) may not necessarily have the largest $\langle \text{SAR} \rangle^{\text{pulse}}$.

Many of the 200-MHz samples have a $\langle \text{SAR} \rangle^{\text{pulse}}$ value, but not necessarily a sequence $\langle \text{SAR} \rangle$ value that is above the FDA 3.2-W/kg limit. As discussed in the Methods section, the 2.0-amp coil current in some of the configurations will result in a shorter RF rectangular pulse than the typical experimental setup of 2.0 ms. These configurations may have an overestimated $\langle \text{SAR} \rangle^{\text{pulse}}$ because the corresponding B_1 field would be stronger than the B_1 field required to produce an optimal image. It was more convenient within this subsection to keep the coil currents the same so the dielectric resonance effects and the quasi-harmonic $\langle \text{SAR} \rangle^{\text{pulse}}$ vs. ϵ_r behavior could be more clearly discussed. For these reasons, the $\langle \text{SAR} \rangle$ values for a pulse sequence were not discussed. Because the SAR is important for safety

Table 2. The $B_{1\rho}(A)$, $\langle \text{SAR} \rangle^{\text{pulse}}$, maximum $\text{SAR}^{\text{pulse}}$ ($\text{SAR}^{\text{pulse}}_{\text{max}}$), and maximum normalized $\text{SAR}^{\text{pulse}}$ (${}^N\text{SAR}^{\text{pulse}}_{\text{max}}$) for the five $B_{1\rho}$, and $\text{SAR}^{\text{pulse}}$ surface plots. The factor necessary to scale the $B_{1\rho}(A)$ value to $3.0 \mu\text{T}$ reduces $\text{SAR}^{\text{pulse}}_{\text{max}}$ by that factor squared

Frequency (MHz)	Samples σ (S/m), ϵ_r	$B_{1\rho}$ (A) (μT) $I_c^* = 2.0$ amp	$\langle \text{SAR} \rangle^{\text{pulse}}$ (W/kg) $I_c^* = 2.0$ amp	$\text{SAR}^{\text{pulse}}_{\text{max}}$ (W/kg) $I_c^* = 2.0$ amp	${}^N\text{SAR}^{\text{pulse}}_{\text{max}}$ (W/kg) Normalized**
10	0.30, 225	3.30	$3.8\text{E} - 3$	$8.2\text{E} - 2$	$6.8\text{E} - 2$
63	0.45, 135	4.20	$3.8\text{E} - 1$	$4.16\text{E} - 0$	$2.8\text{E} - 0$
63	0.15, 270	5.15	$9.3\text{E} - 1$	$1.9\text{E} - 0$	$6.4\text{E} - 1$
200	0.75, 90	4.82	$3.7\text{E} - 0$	$7.7\text{E} + 1$	$2.9\text{E} + 1$
200	0.15, 90	9.92	$5.7\text{E} - 0$	$2.2\text{E} + 1$	$2.0\text{E} - 0$

* I_c is the total current in the surface coil.

** These values are derived by normalizing $B_{1\rho}(A)$ to $3.0 \mu\text{T}$.

considerations, in the next subsection the RF field magnitude at a reference point within the sample will be normalized to that of a 2.0-ms 90° pulse so that the simulation results may be compared to the experimental situation.

Local SAR and B_1 Field Distributions

The B_1 field distribution and the SAR are important field characteristics in MRI. In practice, safety restrictions placed upon the SAR, in addition to $\langle \text{SAR} \rangle$, limit the amount of energy a sample may absorb from an RF coil so that damage to biologic tissue is avoided. Image quality, however, involves the spatial uniformity of $B_{1\rho}$. For these reasons, surface plots of $B_{1\rho}$ and $\text{SAR}^{\text{pulse}}$ are presented in this subsection. In particular, the configurations at 10, 63, and 200 MHz with σ and ϵ_r values closest to neural tissue are presented. These were chosen because a spherical sample most naturally models human head MRI. The slightly large 30-cm diameter was chosen so that results could be compared with known analytical calculations provided by Carlson and Keltner et al.^{13,14} In addition, two other simulations demonstrating strong dielectric resonance, albeit at non-biologic σ and ϵ_r , one at 63 MHz and at 200 MHz, are discussed because high field MRI in the future might support this type of behavior. For convenience, Table 2 contains the magnitude of $B_{1\rho}$ at the reference point A, $B_{1\rho}(A)$, 5 cm inside the sample, along the coil's axis. The $B_{1\rho}(A)$ value will be used to normalize $B_{1\rho}$ (and consequently $\text{SAR}^{\text{pulse}}$) so that all samples have the same flip angle at point A. This allows the direct comparisons of the $\text{SAR}^{\text{pulse}}$ for different configurations (see Methods section). Table 2 also contains the $\langle \text{SAR} \rangle^{\text{pulse}}$ and the maximum of the non-normalized and normalized $\text{SAR}^{\text{pulse}}$ for each configuration presented in this subsection. These numerical $\text{SAR}^{\text{pulse}}$ maxima are an upper limit on what may be expected from this experiment because actual $\text{SAR}^{\text{pulse}}$ measurements are done over finite volumes. Volume-

averaged quantities, such as $\langle \text{SAR} \rangle^{\text{pulse}}$, may be compared directly with the experiment.

10-MHz solutions

Figure 4a shows a shaded surface plot of $B_{1\rho}$ for the sample approximating neural tissue ($\sigma = 0.30$ S/m and $\epsilon_r = 225$), on the x-y-plane containing a cross-section of the phantom. The $B_{1\rho}$ value at the reference point, $B_{1\rho}(A)$, is $3.30 \mu\text{T}$. Because λ is approximately $2.6 \times D_s$, the coil-sample interaction is weak and the field profile approaches that of an RF coil in free space. In fact, all 10 MHz $B_{1\rho}$ distributions are nearly identical. The edge of the sphere's cross-section is superimposed above the $B_{1\rho}$ surface as a thick black circle to aid the eye in visualizing the areas of the field inside the phantom. All of the remaining surface plots have the same orientation with the sphere's cross-sectional edge superimposed over the field surfaces.

The corresponding normalized $\text{SAR}^{\text{pulse}}$, Fig. 4b, has a maximum of $6.80\text{E}-2$ W/kg, well below the FDA 8.0-/kg limit. It occurs near the surface of the sample closest to the coil. The $\text{SAR}^{\text{pulse}}$ is zero along the coil's axis because of the configuration's axial symmetry: consistent with Lenz's law, the magnetic field of the surface coil induces a circulating eddy current in the direction opposite the coil's current which by symmetry must circulate around, and vanish on, the z-axis. The same general features will be observed at 63 and 200 MHz; although with $\lambda < D_s$, part of the eddy current will begin to circulate in the opposite direction (the same direction as the coil's current), at the end of the sample far from the coil. If the eddy currents are of significant amplitude, they produce an inhomogeneous $B_{1\rho}$.

63-MHz Solutions

The $B_{1\rho}$ for the sample representing neural tissue ($\sigma = 0.45$ S/m and $\epsilon_r = 135$), Fig. 5a, has an overall spatial distribution similar to the 10-MHz plot (Fig. 4a) albeit

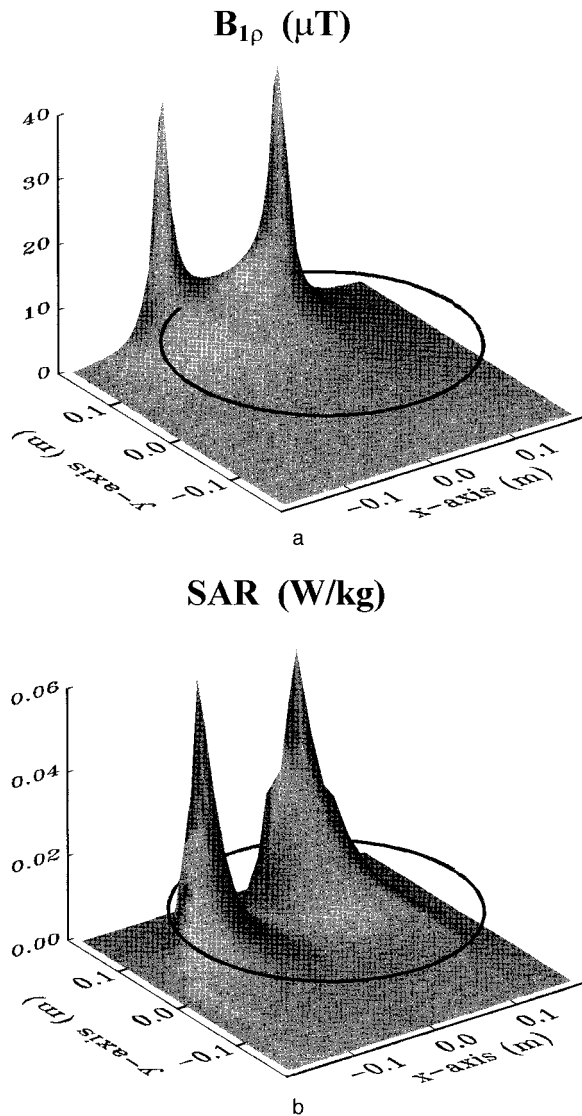


Fig. 4. Surface plots of (a) $B_{1\rho}$ and (b) SAR^{pulse} for the configuration most closely representing neural tissue at 10 MHz ($\sigma = 0.3$ S/m and $\epsilon_r = 225$). The superimposed circle on both plots is the phantom's cross-sectional edge to aid the eye in visualizing which sections of the field fall within the sample. Both figures are similar to the coil in free space (without the phantom) solution.

with a slight increase in field intensity evident by the larger $B_{1\rho}(A)$ value of $4.20 \mu T$. The normalized SAR^{pulse} , Fig. 5b, also similar to the 10-MHz solution (Fig. 4b) is larger by an order of magnitude and its maximum value, occurring near the sphere surface closest to the coil, is 2.84 W/kg.

The $B_{1\rho}$ field and the normalized SAR^{pulse} distribution of a typical resonating sample ($\sigma = 0.15$ S/m and $\epsilon_r = 270$) are shown in Fig. 5c and 5d, respectively. This sample produced the local $\langle SAR \rangle^{pulse}$ maxima on the

$\langle SAR \rangle^{pulse}$ vs. ϵ_r curve in Fig. 2a. The $B_{1\rho}$ field in Fig. 5c is increased near the coil and forms a peak at the center of the sample. This is reflected in a larger $B_{1\rho}(A)$, $5.15 \mu T$, and in the $6.50 \mu T$ $B_{1\rho}$ value at the phantom's center. The $B_{1\rho}$ value at the sample's center is at least five times larger than any of the 10-MHz values. The $B_{1\rho}$ field is produced by the nontrivial eddy current distribution: the current within the half of sample closest to the coil circulates in a direction opposite to the coil's current, whereas the current in other half of the sample flows in the opposite direction. This "bimodal" current pattern is a result of $\lambda \cong D_s$, its direction is given by Lenz's Law, and results in the four distinct regions observed in the SAR^{pulse} data shown in Fig. 5c. The maximum normalized SAR^{pulse} is 0.64 W/kg, well below the 8.0 -W/kg FDA limit, occurs near the sphere's surface closest to the coil. The SAR^{pulse} peaks furthest from the coil have similar values.

The maximum values of the normalized SAR^{pulse} and $\langle SAR \rangle^{pulse}$ may be compared in Table 2. The largest normalized SAR^{pulse} maximum was produced by the non-resonating sample. Its spatial distribution, Fig. 5b, is highly localized in the region of the sample near the coil. During resonance, the SAR^{pulse} increases throughout the majority of the sample, increasing $\langle SAR \rangle^{pulse}$, although the maximum normalized SAR^{pulse} is decreased. The restriction on $\langle SAR \rangle$, therefore, may be the more important safety restriction for resonating samples.

200-MHz solutions

The 200-MHz neural tissue $B_{1\rho}$ ($\sigma = 0.75$ S/m and $\epsilon_r = 90$), Fig. 6a, is similar to the corresponding 63-MHz and 10-MHz plots, except that the intensity is increased ($B_{1\rho}(A) = 4.82 \mu T$). The associated normalized SAR^{pulse} (Fig. 6b) demonstrates the energy absorbed is concentrated in the region near the sample surface next to the coil. The normalized SAR^{pulse} maximum, 29.76 W/kg, is 40 times larger the 63-MHz SAR^{pulse} maximum and exceeds the FDA 8.0 -W/kg limit. If a spin-echo sequence is used with a 2.0 -ms pulse duration for both the 90° and 180° pulses, then Eq. (9) demonstrates that the maximum local SAR for the sequence will exceed the FDA 8.0 -W/kg limit when the repetition time is less than approximately 100 ms. This calculation, however, provides only an upper bound on the expected maximum SAR values because biologic structures in reality are heterogeneous. The boundary between different tissue layers (for example from bone to muscle), would hinder current flow. Current magnitude would be attenuated and less energy would be absorbed by the system. Similarly, poorly conducting superficial lipid layers in the body, which do not easily support eddy currents, would further decrease SAR levels. These results suggest the need for more realistic three-dimensional models, with more complex

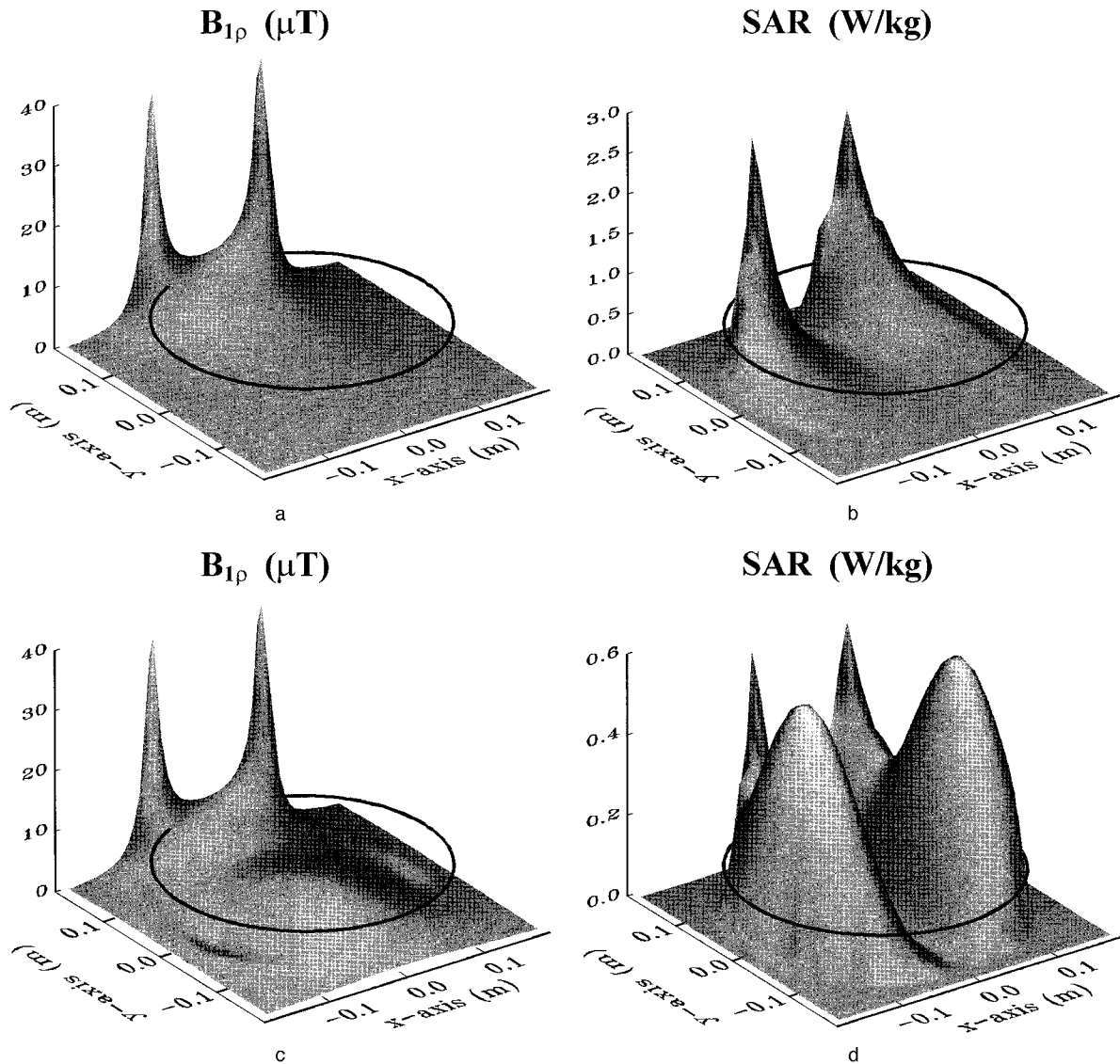


Fig. 5. Surface plots of (a) $B_{1\rho}$ and (b) SAR^{pulse} for the configuration most closely representing neural tissue at 63 MHz ($\sigma = 0.45$ S/m and $\epsilon_r = 135$). The surface plots of (c) $B_{1\rho}$ and (d) SAR^{pulse} for a configuration undergoing dielectric resonance at 63 MHz ($\sigma = 0.15$ S/m and $\epsilon_r = 270$). The $B_{1\rho}$ field in the resonating sample is increased at the sample's center.

geometries, to calculate these high field effects. This study is currently being pursued.

The $B_{1\rho}$ field and SAR^{pulse} dramatically change for the sample with $\sigma = 0.15$ S/m and $\epsilon_r = 90$ (Fig. 6c and d). The corresponding λ satisfies $\lambda \cong D_s/2$ and dielectric resonance occurs. The resultant $B_{1\rho}$ has three maxima along the z -axis and four maxima off axis. This demonstrates that conclusions based on on-axis calculations may not fully describe the coil sensitivity in conductive samples, especially at high frequencies. The $B_{1\rho}$ (A) value of Fig. 6c is $9.99 \mu\text{T}$ which is larger than previous cases studied. The field inhomogeneities in Fig. 6c result from three eddy current "modes": current circulates op-

posite to the coil's current in the third of the sample nearest the coil and in the third of the sample furthest from the coil, whereas current in the middle third flows in the opposite direction. This current pattern results in the six separate areas within the SAR^{pulse} plot of Fig. 6d. The maximum normalized SAR^{pulse} next to the coil is approximately 2.0 W/kg and the value of the peak furthest from the coil is approximately 1.0 W/kg. Both of these values are within the FDA limit.

More complicated $B_{1\rho}$ and SAR^{pulse} were generated (and not shown) for the $\sigma = 0.15$ S/m and $\epsilon_r = 225$ samples. Here λ is near $D_s/3$ and the $\langle SAR \rangle^{\text{pulse}}$ obtains a local maximum already discussed in Fig. 3a. In

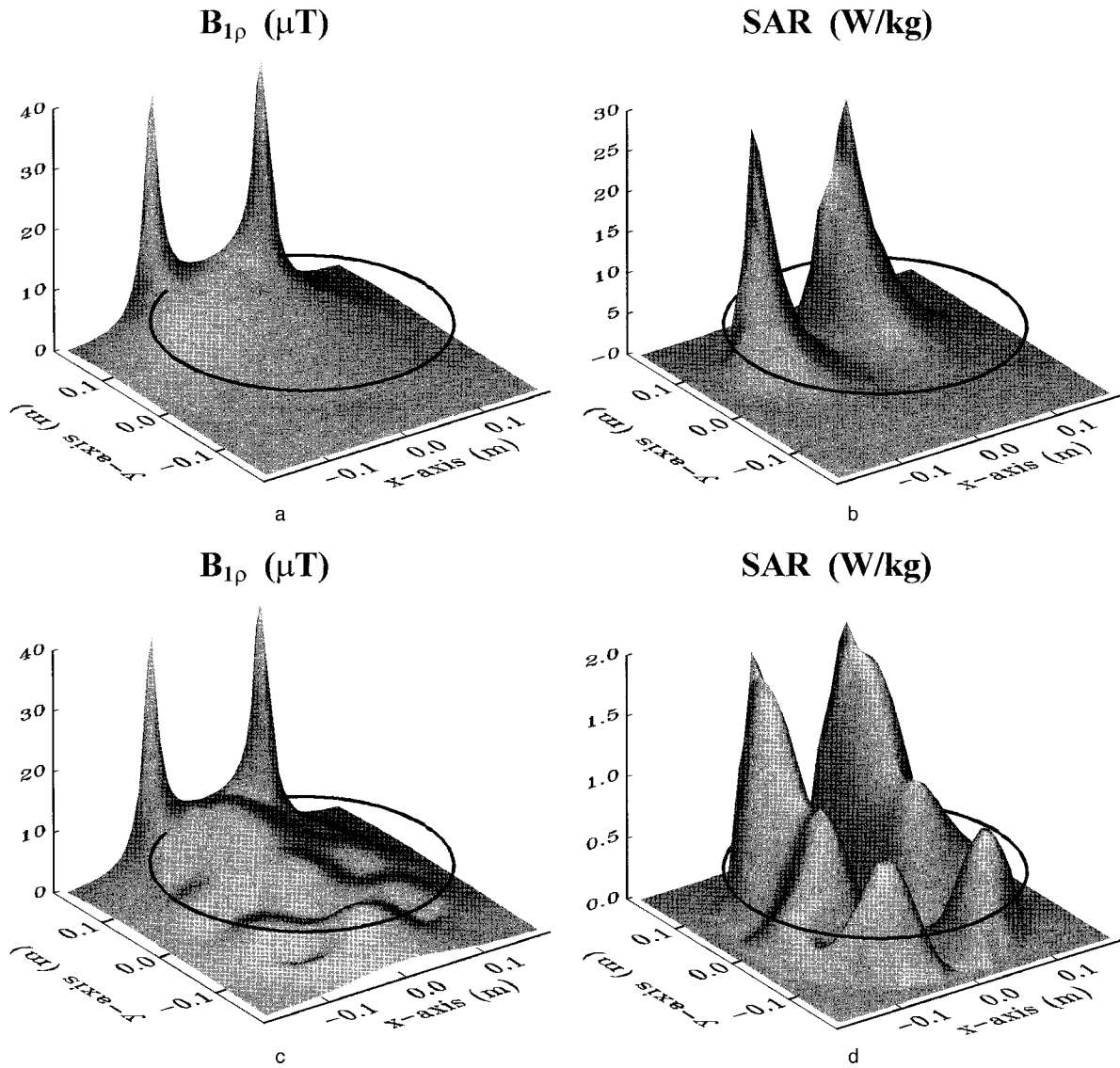


Fig. 6. Surface plots of (a) $B_{1\rho}$ and (b) SAR^{pulse} for the configuration most closely representing neural tissue at 200 MHz ($\sigma = 0.75$ S/m and $\epsilon_r = 90$). The surface plots of (c) $B_{1\rho}$ and (d) SAR^{pulse} for a configuration undergoing dielectric resonance at 200 MHz ($\sigma = 0.15$ S/m and $\epsilon_r = 90$). The $B_{1\rho}$ field in the resonating sample has three maximum along the coil's axis within the phantom, and four off-axis maxima, resulting from a complex eddy current distribution. The SAR^{pulse} in the resonating sample is increased throughout the sample.

this case, there are four $B_{1\rho}$ field peaks along the z -axis and eight SAR^{pulse} maxima inside the sphere.

CONCLUSIONS

A comprehensive numerical study of a spherical phantom next to a surface coil was performed to examine the role of dielectric, wavelength, and skin depth effects on field homogeneity, SAR^{pulse} , $\langle SAR \rangle^{pulse}$, and E_B . These quantities become increasingly important, and less clearly understood, in high field MRI, where the typical analytic approximations become unreliable.

The complex $\langle SAR \rangle^{pulse}$ and E_B vs. ϵ_r behavior, which were analyzed in terms of σ , ϵ_r , λ , δ , and ω , demonstrated an approximate harmonic variation when both the dielectric resonance conditions ($\delta > D_s$ and $D_s \cong n\lambda$) were satisfied. Physically, the incident EM wave reflects off the sphere/air interface, back into the sample, increasing B_1 within parts of the phantom thereby increasing E_B and $\langle SAR \rangle^{pulse}$. Configurations with the largest E_B values did not necessarily have the largest $\langle SAR \rangle^{pulse}$. At 10 MHz, $\delta > D_s$ and $D_s \cong n\lambda$ were never satisfied and the spatial behavior of the B_1 field

was similar to the free space and coil solution; consequently, the E_B values were monotonous and the relatively small $\langle \text{SAR} \rangle^{\text{pulse}}$ values were well below FDA limits and proportional to σ . At 63 MHz, the $\sigma = 0.15$ and 0.30 S/m $\langle \text{SAR} \rangle^{\text{pulse}}$ vs. ϵ_r curves had a local maximum near $\epsilon_r = 275$ where $\lambda \cong D_s \cong 30$ cm. The 63-MHz $\langle \text{SAR} \rangle^{\text{pulse}}$ were of order 1.0 W/kg, all below FDA limits. At 200 MHz, the $\sigma = 0.15$, 0.30, and 0.45 S/m $\langle \text{SAR} \rangle^{\text{pulse}}$ curves had three maxima at $\epsilon_r = 90$, 250, and 405 where $\lambda \cong D_s/2$, $D_s/3$, and $D_s/4$ respectively. With a coil current of 2.0 amps, the majority of the 200-MHz $\langle \text{SAR} \rangle^{\text{pulse}}$, but not necessarily the sequence SAR, were above the FDA 3.2-W/kg limit, albeit for non-biologic σ and ϵ_r values. In general, the 200-MHz $\langle \text{SAR} \rangle^{\text{pulse}}$ are an order of magnitude larger than the 63-MHz $\langle \text{SAR} \rangle^{\text{pulse}}$, as were the 63-MHz $\langle \text{SAR} \rangle^{\text{pulse}}$ an order of magnitude larger than 10-MHz $\langle \text{SAR} \rangle^{\text{pulse}}$. At 63 and 200 MHz, all E_B values at smaller σ or ϵ_r , were strictly less than those E_B values at larger σ or ϵ_r .

The $B_{1\rho}$ surface plots for the samples representing neural tissue were displayed at each frequency. The overall spatial distributions were all similar, albeit with a slight increase in intensity with larger ω . Their maximum normalized $\text{SAR}^{\text{pulse}}$ values, at 10 and 63 MHz, were below the FDA 8.0-W/kg limit. At 200 MHz, however, the maximum normalized $\text{SAR}^{\text{pulse}}$ value was 40 times larger than the 63-MHz value, 29.76 W/kg, which exceeds FDA limits for a spin-echo sequence when the repetition time is less than 100 ms. The 29.76-W/kg $\text{SAR}^{\text{pulse}}$ value is an upper bound because tissue boundary and superficial lipid layers, which would damp eddy current excitations, are not contained within the model. More realistic three dimensional models are needed to evaluate their effects.

In general, samples undergoing dielectric resonance have an increased $\text{SAR}^{\text{pulse}}$. At 200 MHz, the maximum normalized $\text{SAR}^{\text{pulse}}$ within the $\sigma = 0.15$ S/m and $\epsilon_r = 90$ resonating sample was less than the maximum normalized $\text{SAR}^{\text{pulse}}$ for neural tissue. The resonating sample's $\langle \text{SAR} \rangle^{\text{pulse}}$, however, was larger than the neural tissue's $\langle \text{SAR} \rangle^{\text{pulse}}$. This suggests that the $\langle \text{SAR} \rangle$ may be more important at high fields when dielectric resonance occurs. The $\text{SAR}^{\text{pulse}}$ for the neural tissue samples at each frequency were all similar in spatial distribution with the maxima occurring near the sample's surface near the coil.

The 200 MHz $\sigma = 0.15$ S/m, $\epsilon_r = 90$ $B_{1\rho}$ had three maxima along the z -axis and four maxima off axis. These field inhomogeneities were produced from three areas of eddy current, which circulate in alternating directions within different thirds of the sample. This current pattern translated into six $\text{SAR}^{\text{pulse}}$ peaks. The maximum normalized $\text{SAR}^{\text{pulse}}$, next to the coil, was approximately 2.0

W/kg; and the peak furthest from the coil was approximately 1.0 W/kg, both below FDA limits. The off axis $B_{1\rho}$ maxima, important for field homogeneity considerations, demonstrate that on-axis analytic calculations do not fully describe conductive samples, especially at high frequencies values where approximations become increasingly unreliable.

REFERENCES

1. Bottomley, P.A.; Redington, R.W.; Edelstein, W.A.; Schenck, J.F. Estimating radiofrequency power deposition in body NMR imaging. *Magn. Reson. Med.* 2:336–349; 1985.
2. Petropoulos, L.S.; Haacke, E.M. Higher-order frequency dependence of radiofrequency penetration in planar, cylindrical and spherical models. *J. Magn. Reson.* 91:466–474; 1991.
3. Bottomley, P.A.; Andrew, E.R. RF magnetic field penetration, phase shift and power dissipation in biologic tissue: Implication for NMR imaging. *Phys. Med. Biol.* 23:630–643; 1978.
4. Foo, T.K.; Hayes, C.E.; Kang, Y.W. An analytical model for the design of RF resonators for MR body imaging. *Magn. Reson. Med.* 21:165–177; 1991.
5. Petropoulos, L.S.; Haacke, E.M.; Brown, R.W.; Boerner, E. Predicting RF field penetration in heterogeneous bodies using a 3-D finite element approach: Preliminary results. *Magn. Reson. Med.* 30:366–372; 1993.
6. Tofts, P.S. Standing waves in uniform water phantoms. *J. Magn. Reson. B.* 104:143–147; 1994.
7. Lin, J.C. Computer methods for field intensity predictions. In: C. Polk, E. Postow (Eds.). *CRC Handbook of Biologic Effects of Electromagnetic Fields*. Boca Raton: CRC Press. Inc.; 1986: pp. 273–314.
8. Brown, R.W.; Haacke, E.M.; Martens, M.A.; Patrick, J.L.; Zypman, F.R. A layer model for RF penetration, heating, and screening in NMR. *J. Magn. Reson.* 80:225–247; 1988.
9. Tofts, P.S. The distribution of induced currents in magnetic stimulation of the nervous system. *Phys. Med. Biol.* 35: 1119–1128; 1990.
10. Bottomley, P.A.; Roemer, P. Ann. Homogeneous tissue model estimates of RF power deposition in human NMR studies. Local elevations predicted in surface coil decoupling. *N.Y. Acad. Sci. USA* 649:144–159; 1992.
11. Collins, C.M.; Li, S.; Yang, Q.X.; Smith, M.B. Importance of accurate geometry in high-frequency B1 calculations. In: *Proceedings of the International Society for Magnetic Resonance in Medicine*, Vol. 1. New York: ISMRM; 1996: 253.
12. Simunic, D.; Wach, P.; Renhart, W.; Stollberger, R. Spatial distribution of high-frequency electromagnetic energy in human head during MRI: Numerical results and measurements. *IEEE Trans. Biomed. Eng.* 43:88–94; 1996.
13. Carlson, J.W. Radiofrequency field propagation in conductive NMR samples. *J. Magn. Reson.* 78:563–573; 1988.
14. Keltner, J.R.; Carlson, J.W.; Roos, M.; Wong, T.S.; Wong,

- T.L.; Budinger, T.F. Electromagnetic fields of surface coil in vivo NMR at high frequencies. *Magn. Reson. Med.* 22:467–480; 1991.
15. Han, Y.; Wright, S.M. Analysis of RF penetration effects in MRI using finite-difference time-domain method. In: *Proceedings of the Society of Magnetic Resonance in Medicine*, Vol. 3. New York: ISMRH 1992: 1327.
 16. Kritikos, H.N.; Schwan, H.P. Hot spots generated in conducting spheres by electromagnetic waves and biologic implications. *IEEE Trans. Biomed. Eng.* 19:53–58; 1972.
 17. Lin, J.C.; Guy, A.W.; Johnson, C.C. Power deposition in a spherical model of man exposed to 1–20-MHz electromagnetic fields. *IEEE Trans. Microwave Theory Tech.* 12:791–797; 1973.
 18. Johnson, C.C.; Durney, C.H.; Massoudi, H. *IEEE Trans. Microwave Theory Tech.* 23:739–747; 1975.
 19. Harphen, M.D. Influence of skin depth on NMR coil impedance. Part II. *Phys. Med. Biol.* 33:597–605; 1988.
 20. Orcutt, N.; Gandhi, P. A 3-D impedance method to calculate power deposition in biologic bodies subjected to time varying magnetic fields. *IEEE Trans. Biomed. Eng.* 35: 577–583; 1988.
 21. Harphen, M.D. Eddy current disruption: Effect on nuclear magnetic resonance coil impedance and power loss. *Med. Phys.* 16:781–784; 1989.
 22. Li, S.; Yang, Q.X.; Smith, M.B. RF coil optimization: Evaluation of B1 field homogeneity using field histograms and finite element calculations. *Magn. Reson. Imaging.* 12:1079–1087; 1994.
 23. Li, S.; Willams, G.D.; Frisk, T.A.; Arnold, B.W.; Smith, M.B. A computer simulation of the static magnetic field distribution in the human head. *Magn. Reson. Med.* 34: 268–275; 1995.
 24. Li, S.; Dardzinski, B.J.; Collins, C.M.; Yang, Q.X.; Smith, M.B. Three-dimensional mapping of the static magnetic field inside the human head. *Magn. Reson. Med.* 36:705–714; 1996.
 25. Foster, K.R.; Schwan, H.P. Dielectric permittivity and electrical conductivity of biologic materials. In: C. Polk, E. Postow (Eds.) *CRC Handbook of Biologic Effects of Electromagnetic Fields*. Boca Raton: CRC Press. Inc.; 1986: pp. 27–98.
 26. Jones, W.T.; Zhang, Y.; Li, C.; Jirtle, R.L. The measured electrical properties of normal and malignant human tissues from 50 to 90 MHz. *Med Phys.* 21:547–550.
 27. Food and Drug Administration. Magnetic resonance diagnostic device: Panel recommendation and report on petitions for MR reclassification. *Fed. Register.* 53:7575–7579; 1988.
 28. Shellock, F.G.; Kanal, E. *Magnetic Resonance: Bioeffects, Safety, and Patient Management*. New York: Raven Press; 1994: 9–40.